Acta Geotechnica (2020) 15:1637–1653
https://doi.org/10.1007/s11440-019-00873-z

RESEARCH PAPER

Elastoplastic damage seepage–consolidation coupled model of unsaturated undisturbed loess and its application

Zhihua Yao[1] · Zhenghan Chen[2] · Xiangwei Fang[3] · Weiguang Wang[1] · Wan Li[1] · Lihai Su[1]

Received: 15 April 2019 / Accepted: 16 September 2019 / Published online: 9 October 2019

Abstract
The structural characteristic of unsaturated undisturbed loess has a significant impact on its mechanical properties. In this paper, based on the Barcelona basic model of unsaturated soil, an elastoplastic damage model (EDM) of unsaturated undisturbed loess has been developed, which considers the mesostructure evolutions in the loading and collapsing processes. By embedding the new EDM to the seepage–consolidation theory of unsaturated soil and combining it with the water–air migration laws of unsaturated loess, an elastoplastic damage seepage–consolidation coupled model (EDSCM) for the collapsible loess has been developed, which includes the effect of loess structure. Based on the new EDSCM, a new finite element program termed as unsaturated loess elastoplastic damage seepage–consolidation (ULEDSC) has been compiled. The developed program reflects the unique mechanical response of collapsible deformation of loess foundation during the water infiltrating process. Using the ULEDSC, the large-scale field-soaking test has been simulated for two periods, i.e., a 151-day period of wetting and a 251-day period of drying. The numerical results show that the propagation of wetting front is identical to a pumpkin-shaped zone. Due to the self-weight of collapsible loess and water, slow water filtration resulted in loess collapses and vertical displacement. The vertical displacement during the subsequent drying stage is mainly caused by the loess collapse and consolidation settlements of the shallow soil layer below the bottom of the test pit. The numerically simulated results from ULEDSC are in accordance with the field monitoring data, which also show the multi-field coupling response in the self-weight collapsible loess foundation during the initial wetting and subsequent drying periods. The new models and the finite element program could provide some scientific references for solving the engineering problems of self-weight collapsible loess in Midwestern China.

Keywords Collapsible deformation · Damage · Multi-field coupling · Structure · Undisturbed loess · Unsaturated

1 Introduction

In recent years, large-scale construction projects in the loess areas of Midwestern China have increased the understanding of collapsible deformation of self-weight collapsible loess [23, 35]. Large-scale soaking tests had been carried out on some important projects, which consisted of typical multi-field coupling process, including the collapsibility, water–air migration and structural damage. It is necessary to consider all these factors in order to fully understand the multi-field coupling problems. At present, there are only a few reports on the multi-field coupling response of self-weight collapsible loess foundation during the water infiltrating periods.

It is well known that under the condition of loading and infiltrating processes, the unsaturated undisturbed loess can produce irreversible collapsible deformation, which is closely related to the loess structure [11, 29]. When the loess structure is not damaged or softened, the undisturbed loess has the characteristics of lower compressibility and higher strength. Once the loess structure is damaged, its mechanical properties are susceptible to yielding,

✉ Xiangwei Fang
fangxiangwei1975@163.com

[1] Department of Airdrome Construction Engineering, Air Force Engineering University, Xi'an 710038, People's Republic of China

[2] Department of Civil Engineering, Logistical Engineering University, Chongqing 401311, People's Republic of China

[3] School of Civil Engineering, Chongqing University, Chongqing 400045, People's Republic of China

softening, and collapsing effect. Loess structure is one of the important fundamental factors while determining the mechanical characteristics of undisturbed loess. It is important to develop a constitutive model considering the soil structure so as to investigate the mechanical characteristics of undisturbed soil [20, 27, 39]. However, many constitutive models of unsaturated soils fail to reflect the structural properties of loess and have neglected the effect of the structure on the collapsible deformation [14, 32–34].

The constitutive model of unsaturated soil is embedded in the multi-field consolidation coupling theory, and this is a good way to solve the mechanical problems in practical engineering projects [2, 19, 21]. This approach is also applicable to collapsible loess. The multi-field coupling effects of collapsible loess on the mechanical characteristics were reported in some previous studies [7, 16, 18, 26]. Nevertheless, these studies did not consider the structural characteristics of collapsible loess during the loading and infiltrating processes. In particular, the effect of the structural characteristics on the collapsible deformation of loess foundation was not sufficiently considered. Therefore, it is of great practical significance to develop the structural constitutive model of collapsible loess, which can be used to explore the multi-field coupling mechanism on collapsible deformation of loess foundation.

Based on BBM [1], and the mesostructure evolution equation obtained by the loading and wetting test using computed tomography technology [38], the objective of this study is to develop a model (EDM) of unsaturated undisturbed loess, which reflects the effect of loess structure on the mechanical characteristics. The model combined with the water–air migration equations of unsaturated loess [36, 37] has been incorporated into the unsaturated seepage consolidation theory [6]. Then, a new coupled model (EDSCM) for the collapsible loess considering the elastoplastic damage evolution has been developed in this paper. The coupled model could reflect the unique mechanical properties of collapsible loess during the loading and wetting processes.

Based upon some previous research results [3, 6, 22], a new finite element program (ULEDSC) for unsaturated loess foundation has been compiled in this paper. Taking the large-scale field-soaking test at Heping town, Lanzhou city, Gansu Province in China, as an example [35], the multi-field coupling response during the collapsing process has been simulated by the new program (ULEDSC) for two periods, i.e., an initial 151-day period of wetting and a subsequent 251-day period of drying. In this way, the results of the simulations could show the multi-field coupling characteristics in relation to the water content field, pore air and water pressure field, displacement field, and damage field. In this paper, the developed new models (EDM and EDSCM) and the new program (ULEDSC) could analyze the multi-field coupling problems of collapsible loess foundation more effectively.

2 The EDM of unsaturated undisturbed loess

There are two parts in the EDM: One is the soil skeleton, and the other is the water phase. (1) For the soil skeleton phase, the BBM of unsaturated soil has been used to describe the mechanical characteristics of the remolded loess [1]. The structural evolution equations have been used to describe the loading and collapsing processes, which represent the structural characteristics of undisturbed loess [38]. (2) For the changes of water phase, in order to consider the effect of net mean stress and deviatoric stress on the water retention characteristics, the generalized soil–water characteristic curve has been used to describe the water retention characteristics.

2.1 Elastic deformation

The expressions for the elastic volumetric strain $\mathrm{d}\varepsilon_v^e$ and elastic deviatoric strain $\mathrm{d}\varepsilon_s^e$ are given by Eqs. (1) and (2), respectively.

$$\mathrm{d}\varepsilon_v^e = \mathrm{d}\varepsilon_{\mathrm{vp}}^e + \mathrm{d}\varepsilon_{\mathrm{vs}}^e = \frac{\kappa}{v}\frac{\mathrm{d}p}{p} + \frac{\kappa_s}{v}\frac{\mathrm{d}s}{s + p_{\mathrm{atm}}} \tag{1}$$

$$\mathrm{d}\varepsilon_s^e = \frac{\mathrm{d}q}{3G} \tag{2}$$

where $\varepsilon_{\mathrm{vp}}^e$ and $\varepsilon_{\mathrm{vs}}^e$ are the elastic volumetric strain related to net mean stress and matric suction, respectively, κ is the elastic stiffness coefficient related to the loading state of the net mean stress, κ_s is the elastic stiffness coefficient related to the increasing suction, G is the shear modulus, p_{atm} is the atmospheric pressure, v is the specific volume of soil, p is the net mean stress, s is the matric suction, and q is the deviatoric stress.

2.2 Plastic properties

The net mean stress p, deviatoric stress q, and suction s can generate deformation of undisturbed loess. Furthermore, the structure of undisturbed loess also has an impact on the mechanical characteristics. Hence, it is assumed that there are two parts in the yielding stress p_y of undisturbed loess, i.e., one is related to the remolded loess and the other is related to the loess structure. The first part of remolded loess is still in accordance with the BBM [1]. The second part is described by the law of structural evolution [38]. So, the yield stress p_y of undisturbed soil is given by:

$$p_y = p_0 + p^s m_{1\sigma} \tag{3}$$

where p_0 is the net mean stress of remolded loess. p^s is the difference of the net mean stress between undisturbed soil sample and remolded soil sample under the same condition of dry density and initial suction. $m_{1\sigma}$ is the structural parameter for the loading process. The expressions for p^s, p_0, and $m_{1\sigma}$ are given by Eqs. (4)–(7), respectively:

$$p^s = p_{ci} - p_{0i} \tag{4}$$

$$\left(\frac{p_0}{p^c}\right) = \left(\frac{p_0^*}{p^c}\right)^{\frac{\lambda(0)-\kappa}{\lambda(s)-\kappa}} \tag{5}$$

$$\lambda(s) = \lambda(0)[(1-r)\exp(-\beta s) + r] \tag{6}$$

$$m_{1\sigma} = m_{1o}(1 - D_1) \tag{7}$$

where p_{ci} and p_{0i} are the initial yielding net mean stress of undisturbed soil and remolded soil, respectively. p^c is the reference stress. p_0^* is the reconsolidation pressure of saturated soil. $\lambda(s)$ is the stiffness parameter for changes in net mean stress for virgin states of the soil. $\lambda(0)$ is the slope of the virgin saturated consolidation line. r and β are model parameters, i.e., $r = \lambda(s \to \infty)/\lambda(0)$. m_{1o} is the initial structural parameter. D_1 is the structural damage variable during loading process, and its expression is Eq. (15).

During the wetting process, as the suction decreases, the structural damage of undisturbed loess equals to D_2, as shown by Eq. (16). Under this condition, there is no further structural damage. Hence, the structural damage variable D_1 is fixed as the $D_{1\sigma}$. The subscript 1σ indicates that the stress state is σ. At any moment during the collapsing process, the structural damage variable D is given by:

$$D = D_{1\sigma} + D_2 \tag{8}$$

The structural parameter $m_{1\sigma w}$ in the collapsing process is defined as:

$$m_{1\sigma w} = m_{1o}(1 - D_{1\sigma} - D_2) \tag{9}$$

During the collapsing process, the natural structure of undisturbed soil is destroyed gradually, and the characteristics of the undisturbed soil transform slowly into that of the remolded soil. Based on the composite damage theory [8], the critical state line M_{fsh} during the collapsing process can be determined as follows:

$$M_{\mathrm{fsh}} = (1 - D)M^* + DM \tag{10}$$

where M^* is the slope of the critical state line of the undisturbed soil and M is the slope of the critical state line of the remolded soils.

From Eq. (10), it can be seen that for $D_1 = 0$, as expressed in Eq. (15), there is no structural damage in the soil sample. Under this condition, $M_{\mathrm{fsh}} = M^*$. For $D_1 = 1$, the soil sample changes to the remolded sample, and $M_{\mathrm{fsh}} = M$. For $0 < D_1 < 1$, when the loess sample is subjected to the external load and water, it is not completely destroyed. The sample is in the intermediate transforming state from the undisturbed soil to the remolded soil. If the external load is not taken into account, the damage variable is directly transformed to D_2 during the collapsing process.

Substituting Eqs. (3) and (10) into the load–collapse (LC) yield surface equation [1], the LC yield surface considering the effect of structure on the loading and collapsing process can be written as:

$$f(p, q, s, p_s^*) \equiv q^2 - M_{\mathrm{fsh}}^2(p + p_s^*)(p_y - p) = 0 \tag{11}$$

where p is the net mean stress, q is the deviatoric stress, and p_s^* is the intercept of the critical state lines in the axis of net mean stress for undisturbed loess.

In this paper, the effect of the structure on the suction increase (SI) yield surface temporarily has not been considered [4]. The associated flow rule has been used in the loading and collapsing processes. By combining the hardening law with Eqs. (3) and (5), the incremental yield stress $\mathrm{d}p_y$ is expressed as follows:

$$\mathrm{d}p_y = \frac{\lambda(0) - \kappa}{\lambda(s) - \kappa} \cdot \left(\frac{p_0^*}{p^c}\right)^{\frac{\lambda(0)-\lambda(s)}{\lambda(s)-\kappa}} \mathrm{d}p_0^* + p^s \mathrm{d}m_{1\sigma w} \tag{12}$$

where

$$\frac{\mathrm{d}p_0^*}{p_0^*} = \frac{v}{\lambda(0) - \kappa} \mathrm{d}\varepsilon_v^p \tag{13}$$

$$\mathrm{d}m_{1\sigma w} = -m_{1o}\mathrm{d}D_2 \tag{14}$$

Equation (12) is applicable to the same conditions of initial dry density and water content of the remolded soil and undisturbed soil. With increasing structural damage, the hardening parameter p_y decreases, which reflects the softening properties due to the natural structure damage. Furthermore, p_0^* increases with the increase in volumetric strain, which reflects the damage of original structure and the hardening characteristics of a new structure in Eq. (12).

2.3 Structural damage evolution equation

Zhu [38] analyzed the mesostructure of unsaturated undisturbed loess under the loading and collapsing processes. The damage evolution equations clearly demonstrate the evolutionary characteristics of structural damage and clarify the transformation process of undisturbed loess from non-damage state to complete damage state. The damage evolution equations for the loading and collapsing processes are represented by Eqs. (15) and (16), respectively.

$$D_1 = A^1\langle \varepsilon_{\mathrm{v}} - \varepsilon_{\mathrm{vc}} \rangle + A^2\langle \varepsilon_{\mathrm{s}} - \varepsilon_{\mathrm{sc}} \rangle \tag{15}$$

$$D_2 = 1 - \exp\left[-\left(A^3\varepsilon_{\mathrm{v}}^{\mathrm{sh}} + A^4\varepsilon_{\mathrm{s}}^{\mathrm{sh}} + A^5\right)\frac{\theta - \theta_\sigma}{\theta_{\mathrm{s}} - \theta_\sigma}\right] \tag{16}$$

where ε_v is the summation of volumetric strain in the consolidation and shearing process. ε_s is the deviatoric strain in the shearing process. ε_{vc} and ε_{sc} are the initial volumetric strain and initial shear strain, respectively. $\varepsilon_{vc} = 0.017$, and $\varepsilon_{sc} = 0.01$. θ is the volumetric water content. θ_s is the volumetric water content when loess sample is saturated. θ_σ is the volumetric water content before wetting, and A^1, A^2, A^3, A^4, and A^5 are the fitting parameters and have the values of: $A^1 = 1.33$, $A^2 = 1.27$, $A^3 = 24.16$, $A^4 = 3.07$, and $A^5 = 0.54$, respectively.

2.4 Water retention characteristics

The water phase can be described using the generalized soil–water characteristic curve [10], which considers the effect of the net mean stress and deviatoric stress, and the expression is as follows:

$$\mathrm{d}\varepsilon_w = \frac{\mathrm{d}p}{K_{\mathrm{wpt}}} + \frac{\mathrm{d}s}{H_{\mathrm{wt}}} + \frac{\mathrm{d}q}{K_{\mathrm{wqt}}} \tag{17}$$

where K_{wpt}, H_{wt}, and K_{wqt} are the tangent moduli of the water phase related to the net mean stress, suction stress, and deviatoric stress, respectively [31].

2.5 The relationship between stress and strain

In this paper, the effect of the structure on the suction increase (SI) yield surface has not been considered. Thus, the new EDM of unsaturated undisturbed loess considering the structural effects is written as a matrix, as follows:

$$\{\mathrm{d}\boldsymbol{\sigma}'\} = \left[\mathbf{D}_{\mathrm{ep}}^{\mathrm{sh}}\right]\{\mathrm{d}\boldsymbol{\varepsilon}\} + \{\mathbf{F}_{\mathrm{esp}}\}\mathrm{d}s \tag{18}$$

where

$$\left[\mathbf{D}_{\mathrm{ep}}^{\mathrm{sh}}\right] = [\mathbf{D}_{\mathrm{e}}] - \frac{[\mathbf{D}_{\mathrm{e}}]\left(\left\{\frac{\partial f}{\partial \boldsymbol{\sigma}'}\right\} + \{\mathbf{m}\}\frac{\partial f}{\partial s}\right)\left\{\frac{\partial f}{\partial \boldsymbol{\sigma}'}\right\}^T[\mathbf{D}_{\mathrm{e}}]}{\left(\left\{\frac{\partial f}{\partial \boldsymbol{\sigma}'}\right\} + \{\mathbf{m}\}\frac{\partial f}{\partial s}\right)\left(\left\{\frac{\partial f}{\partial \boldsymbol{\sigma}'}\right\}^T[\mathbf{D}_{\mathrm{e}}] - \frac{\partial f}{\partial H}\frac{\partial H}{\partial \varepsilon_v^p}\{\mathbf{m}\}^T\right)} \tag{19}$$

$$\{\mathbf{F}_{\mathrm{esp}}\} = \{\mathbf{F}_{\mathrm{es}}\} - \frac{[\mathbf{D}_{\mathrm{e}}]\left(\frac{\partial f}{\partial s} + \left\{\frac{\partial f}{\partial \boldsymbol{\sigma}'}\right\}^T\{\mathbf{F}_{\mathrm{es}}\}\right)\left(\left\{\frac{\partial f}{\partial \boldsymbol{\sigma}'}\right\} + \{\mathbf{m}\}\frac{\partial f}{\partial s}\right)}{\left(\left\{\frac{\partial f}{\partial \boldsymbol{\sigma}'}\right\} + \{\mathbf{m}\}\frac{\partial f}{\partial s}\right)\left(\left\{\frac{\partial f}{\partial \boldsymbol{\sigma}'}\right\}^T[\mathbf{D}_{\mathrm{e}}] - \frac{\partial f}{\partial H}\frac{\partial H}{\partial \varepsilon_v^p}\{\mathbf{m}\}^T\right)} \tag{20}$$

where $[\mathbf{D}_{\mathrm{e}}]$ is an elastic modulus matrix. H is the hardening parameter, which represents the plastic volumetric strain ε_v^p. $\{\mathbf{m}\} = \{1\ \ 1\ \ 1\ \ 0\ \ 0\ \ 0\}^T$. $\left[\mathbf{D}_{\mathrm{ep}}^{\mathrm{sh}}\right]$ is the elastoplastic modulus matrix of unsaturated undisturbed loess considering the effect of the structure $\{\mathbf{F}_{\mathrm{es}}\}$ is the elastic suction modulus matrix of unsaturated undisturbed loess. $\{\mathbf{F}_{\mathrm{esp}}\}$ is the elastoplastic suction modulus matrix of unsaturated undisturbed loess. $\mathbf{f}$ is represented by Eq. (11).

3 The EDSCM of unsaturated undisturbed loess

3.1 Basic equations

There are four basic equations in the EDSCM of unsaturated undisturbed loess, i.e., the equilibrium equation, the continuity equation, the geometric equation, and the constitutive equation. The equations are shown as follows.

3.1.1 Equilibrium equation

There are three independent equilibrium equations of unsaturated soil, i.e., the general equilibrium equation, the equilibrium equation of the liquid phase, and the equilibrium equation of the air phase. All the equilibrium equations have been developed by using dependent variables, such as pore water pressure, pore air pressure, and the velocity of each phase. The three independent equilibrium equations are given below.

The general equilibrium equation is

$$\frac{\partial}{\partial x_j}\left(\boldsymbol{\sigma}_{ij} - u_{\mathrm{a}}\boldsymbol{\delta}_{ij}\right) + \frac{\partial u_{\mathrm{a}}\boldsymbol{\delta}_{ij}}{\partial x_j} + \mathbf{f}_{0i} = 0 \tag{21}$$

where $\boldsymbol{\sigma}_{ij}$ is the stress tensor (i, j = 1, 2, 3). $\mathbf{f}_{0i}$ is the volume force (i = 1, 2, 3). u_a is the pore air pressure and $\boldsymbol{\delta}_{ij}$ is Kronecker sign (i, j = 1, 2, 3).

The equilibrium equation of the liquid phase is

$$\theta(\mathbf{v}_{\mathrm{w}i} - \mathbf{v}_{si}) = -k_{\mathrm{w}}\frac{\partial}{\partial x_i}\left(\frac{u_{\mathrm{w}}}{r_{\mathrm{w}}} + y\right) \tag{22}$$

where k_{w} is the unsaturated hydraulic conductivity related to the matrix suction. θ is the volumetric water content. u_{w} is the pore water pressure $\mathbf{v}_{\mathrm{w}i}$ is the velocity vector of the liquid phase (i = 1, 2, 3). $\mathbf{v}_{si}$ is the velocity vector of the solid phase(i = 1, 2, 3). r_{w} is the unit weight of water, and y is the water head.

The equilibrium equation of air phase is

$$(n - \theta)(\mathbf{v}_{\mathrm{a}i} - \mathbf{v}_{si}) = -k_{\mathrm{a}}\frac{\partial}{\partial x_i}\left(\frac{u_{\mathrm{a}}}{r_{\mathrm{w}}}\right) \tag{23}$$

where k_a is the unsaturated permeability coefficients related to the matrix suction. $\mathbf{v}_{\mathrm{a}i}$ is the velocity vector of the air phase (i = 1, 2, 3). n is the porosity factor.

Water and gas migrations in unsaturated soil are important processes in the seepage–consolidation coupling analysis. The unsaturated hydraulic conductivity k_{w} and the unsaturated permeability coefficient k_{a} are dependent on

the matric suction. In this paper, by combining the water and air migration in unsaturated loess [36, 37] with the soil–water characteristic curve [28], the equations for unsaturated hydraulic conductivity and permeability coefficient of unsaturated undisturbed loess are as follows:

$$k_{\mathrm{w}} = \exp\left\{\eta_{\mathrm{A}} + \frac{\eta_{\mathrm{B}}(1+e)}{e}\left\{\theta_{\mathrm{r}} + \frac{\theta_{\mathrm{s}} - \theta_{\mathrm{r}}}{\left[1 + (\alpha s)^{\overline{n}}\right]^{m}}\right\}\right\} \tag{24}$$

$$k_{\mathrm{a}} = k_{\mathrm{da}} \exp\left\{\xi\left\{\theta_{\mathrm{r}} + \frac{\theta_{\mathrm{s}} - \theta_{\mathrm{r}}}{\left[1 + (\alpha s)^{\overline{n}}\right]^{m}}\right\}^{\zeta}\right\} \tag{25}$$

where η_A, η_B, ξ, and ζ are the fitting parameters, respectively. $\eta_A = -0.0437$ cm/s, $\eta_B = 0.111$ cm/s, $\xi = -2.91$, and $\zeta = 1.75$. θ_r is the residual volumetric water content, $\theta_r = 0.0593$ cm^3/cm^3. θ_s is the volumetric water content of the saturated loess sample, $\theta_s = 0.554$ cm^3/cm^3. α, m and $\overline{n}$ are the fitting parameters, $m = 1 - 1/\overline{n}$, $\alpha = 0.043$ kPa^{-1}, $m = 0.682$, and $\overline{n} = 3.148$. e is the initial void ratio. k_{da} is the initial permeability coefficient of unsaturated undisturbed loess, $k_{\mathrm{da}} = 0.015$ cm/s [31].

3.1.2 Continuity equation

In accordance with the mass conservation equation and the generalized Darcy's law for the source/sink conditions, the continuity equations for the solid, liquid, and air phases of unsaturated soil are expressed as follows, respectively.

The continuity equation for the solid phase is

$$\frac{\partial}{\partial t}(1-n) + \nabla \cdot [(1-n)\mathbf{v}_{si}] = 0 \tag{26}$$

The continuity equation for the liquid phase is

$$\frac{\partial}{\partial t}\theta + \nabla \cdot (\theta \cdot \mathbf{v}_{wi}) = -q_{\mathrm{w}} \tag{27}$$

where q_{w} is the water flow per unit area.

The continuity equation for the air phase is

$$\frac{\partial}{\partial t}\left[(n-\theta)P_{\mathrm{g}}\right] + \nabla \cdot \left[(n-\theta)P_{\mathrm{g}}\mathbf{v}_{ai}\right] = -q_{\mathrm{a}} \tag{28}$$

where $p_g = u_{\mathrm{a}} + p_{\mathrm{atm}}$. p_{atm} is the atmospheric pressure. q_{a} is the air flow per unit area.

In order to simplify the derivation and computation, the velocity vectors of the solid, liquid, and air phases can be rewritten. The divergence expression of the solid phase velocity vector in Eq. (26) is

$$\nabla \cdot \mathbf{v}_{si} = -\boldsymbol{\delta}_{ij}\frac{\partial \boldsymbol{\varepsilon}_{ij}}{\partial t} \tag{29}$$

where $\boldsymbol{\varepsilon}_{ij}$ is the strain tensor (i, j = 1, 2, 3).

The divergence expression of the liquid phase velocity vector in Eq. (27) is

$$\mathbf{v}_{wi} = -\frac{k_{\mathrm{w}}}{r_{\mathrm{w}}}(\nabla \cdot u_{\mathrm{w}} - r_{\mathrm{w}}\boldsymbol{\delta}_{ij,j}) \tag{30}$$

The divergence expression of the air phase velocity vector in Eq. (28) is

$$\mathbf{v}_{ai} = -\frac{k_{\mathrm{a}}}{r_{\mathrm{a}}}(\nabla \cdot u_{\mathrm{a}} - r_{\mathrm{a}}\boldsymbol{\delta}_{ij,j}) \tag{31}$$

where r_{a} is the unit weight of air.

3.1.3 Geometric equation

In a plane strain problem, the strain tensor $\boldsymbol{\varepsilon}_{ij}$ can be used in the geometric equation, and its expression is

$$\boldsymbol{\varepsilon}_{ij} = -\frac{1}{2}\left(\frac{\partial u_{si}}{\partial x_j} + \frac{\partial u_{sj}}{\partial x_i}\right) \tag{32}$$

where u_{si} and u_{sj} are the displacement components of solid phase in horizontal and vertical directions, respectively. The minus sign "-" is used to convert compression into a positive value.

3.1.4 Constitutive equation

There are two parts in the constitutive equation of the damage seepage–consolidation model, i.e., for the solid phase and the liquid phase. With reference to Eq. (18), the constitutive equation for the solid phase is

$$\Delta\boldsymbol{\sigma}'_{ij} = \boldsymbol{D}^{\mathrm{ep}}_{ijkl}\Delta\boldsymbol{\varepsilon}_{kl} + \boldsymbol{F}_{i,j}\mathrm{d}\boldsymbol{s}\delta_{ij} = [\boldsymbol{D}]_{\mathrm{dmg}}[\Delta\boldsymbol{\varepsilon}] + [\boldsymbol{F}]_{\mathrm{dmg}}[\mathrm{d}\boldsymbol{s}] \tag{33}$$

where $\mathbf{D}^{\mathrm{ep}}_{ijkl}$ is an elastic–plastic damage modulus matrix for strain-dependent in loading and wetting processes, which can be written in matrix form $[\mathbf{D}]_{\mathrm{dmg}}$. $\mathbf{F}_{i,j}$ is an elastic–plastic damage modulus matrix for matric suction-dependent, which can be written in matrix form $[\mathbf{F}]_{\mathrm{dmg}}$.

Using Eq. (17) to describe the change in the water phase, and expressing the net mean stress increment as $\mathrm{d}p = \mathrm{d}(\sigma_m - u_a)$, Eq. (17) can be written in an incremental form, as follows:

$$\Delta\varepsilon_{\mathrm{w}} = \frac{\Delta(\sigma_m - u_{\mathrm{a}})}{K_{\mathrm{wpt}}} + \frac{\Delta(u_{\mathrm{a}} - u_{\mathrm{w}})}{H_{\mathrm{wt}}} + \frac{\Delta q}{K_{\mathrm{wqt}}} \tag{34}$$

To simplify the calculations, the constitutive equations for the solid phase and the liquid phase are both rewritten in terms of the incremental quantities. Substituting Eqs. (32) and (33) into Eq. (21) gives:

$$\begin{aligned} &-\frac{1}{2}\left[D_{ijkl}\left(\frac{\partial u_k}{\partial x_l} + \frac{\partial u_l}{\partial x_k}\right)\right]_{,j} + \mathbf{F}_{i,j}(\Delta u_a - \Delta u_w)\delta_{ij} \\ &+ \left(\mathbf{F}_i\boldsymbol{\delta}_{ij} + 1\right)\cdot\Delta u_{a,j} - \mathbf{F}_i\boldsymbol{\delta}_{ij}\Delta u_{w,j} + \mathbf{f}_{0i} = 0 \end{aligned} \tag{35}$$

$$\frac{\partial \boldsymbol{D}_{iikl}\left(\frac{\partial u_k}{\partial x_l}+\frac{\partial u_l}{\partial x_k}\right)}{6K_{\mathrm{wpt}}\partial t}+\frac{[\boldsymbol{L}]\partial \boldsymbol{D}_{ijkl}\left(\frac{\partial u_k}{\partial x_l}+\frac{\partial u_l}{\partial x_k}\right)}{2K_{\mathrm{wqt}}\partial t}-\left(\frac{\boldsymbol{F}_i m_i}{3K_{\mathrm{wpt}}\partial t}+\frac{1}{H_{\mathrm{wt}}\partial t}+\frac{[\boldsymbol{L}]\boldsymbol{F}_i m_i}{K_{\mathrm{wqt}}}\right)\times\frac{\partial\Delta(u_{\mathrm{a}}-u_{\mathrm{w}})}{\partial t}+\nabla\cdot\theta\Delta\mathbf{v}_{\mathrm{si}}-\nabla\cdot k_{\mathrm{w}}\frac{\partial}{\partial x_i}\left(\frac{\Delta u_{\mathrm{w}}}{r_{\mathrm{w}}}+y\right)+q_{\mathrm{w}}=0 \tag{36}$$

$$-\frac{\partial\left[D_{iikl}\left(\frac{\partial u_k}{\partial x_l}+\frac{\partial u_l}{\partial x_k}\right)\right]}{6K_{wpt}\partial t}-\frac{[L]\cdot\partial\left[D_{ijkl}\left(\frac{\partial u_k}{\partial x_l}+\frac{\partial u_l}{\partial x_k}\right)\right]}{2K_{wqt}\partial t}+\left(\frac{F_i m_i}{3K_{wpt}\partial t}+\frac{1}{H_{wt}\partial t}+\frac{[L]F_i m_i}{K_{wqt}}\right)\times\frac{\partial\Delta(u_a-u_w)}{\partial t}+\nabla\cdot[(1-\theta)v_{si}]+\frac{(n-\theta)}{P_g}\frac{\partial u_a}{\partial t}+q_a=\nabla\cdot\left[\frac{k_a}{r_w}\frac{\partial u_a}{\partial x_i}\right] \tag{37}$$

where the matrix [**L**] is introduced to facilitate the computation.

$$[\mathbf{L}]=\sqrt{\frac{2}{q}}\cdot\begin{bmatrix}2\sigma_x-\sigma_y-\sigma_z & 2\sigma_y-\sigma_z-\sigma_x & \\ 2\sigma_z-\sigma_x-\sigma_y & 6\tau_{xy} & 6\tau_{yz} \quad 6\tau_{zx}\end{bmatrix} \tag{38}$$

where σ_x, σ_y, and σ_z represent normal stress in x-, y-, and z-coordinates, respectively. τ_{xy}, τ_{yz}, and τ_{zx} represent shear stress in different directions, respectively.

Equations (35)–(37) represent the governing equations of unsaturated seepage consolidation. Each equation contains five unknown quantities, which fully reflects the coupling effects of the stress, strain, water seepage, air permeation, and structure damage. Substituting Eq. (24) into Eq. (36) and Eq. (25) into Eq. (37), the effect of matric suction variation on the unsaturated hydraulic conductivity and the unsaturated gas permeability coefficient can then be considered. As all the governing equations (Eqs. 35–37) are in terms of the incremental quantities, and assuming the material parameters are constants in each increment calculation, the increment can then be adjusted according to the actual stress and deformation. The elastoplastic damage matrix elements and the suction matrix elements are adjusted to reflect the actual state of the soil according to the stress state.

3.2 Plane consolidation model of unsaturated undisturbed loess

In order to simplify the calculation methods and the mathematical models, the complex three-dimensional problem has been reduced to a plane problem. In this section, the governing equation, Eq. (21), is transformed into two-dimensional coordinates, in which the elements in the z-axis direction are not considered. By combining the continuity equation with the matrix form, the elastoplastic constitutive relation of soil skeleton can be written as follows:

$$D_{11}\frac{\partial^2 u}{\partial x^2}+D_{44}\frac{\partial^2 u}{\partial y^2}+D_{14}\frac{\partial^2 v}{\partial x^2}+D_{42}\frac{\partial^2 v}{\partial y^2}+(D_{12}+D_{44})\frac{\partial^2 v}{\partial x\partial y}+(D_{14}+D_{41})\frac{\partial^2 u}{\partial x\partial y}-\left[(F_1+1)\frac{\partial}{\partial x}+F_4\frac{\partial}{\partial y}\right]\Delta u_a+\left(F_1\frac{\partial}{\partial x}+F_4\frac{\partial}{\partial y}\right)\Delta u_{\mathrm{w}}-f_{0x}=0 \tag{39}$$

$$D_{41}\frac{\partial^2 u}{\partial x^2}+D_{44}\frac{\partial^2 v}{\partial x^2}+D_{24}\frac{\partial^2 u}{\partial y^2}+D_{22}\frac{\partial^2 v}{\partial y^2}+(D_{44}+D_{21})\frac{\partial^2 u}{\partial x\partial y}+(D_{42}+D_{24})\frac{\partial^2 v}{\partial x\partial y}-\left[(F_2+1)\frac{\partial}{\partial y}+F_4\frac{\partial}{\partial x}\right]\Delta u_a+\left(F_4\frac{\partial}{\partial x}+F_2\frac{\partial}{\partial y}\right)\Delta u_w-f_{0y}=0 \tag{40}$$

$$a_1\frac{\partial}{\partial t}\frac{\partial u}{\partial x}+a_2\frac{\partial}{\partial t}\frac{\partial v}{\partial y}+a_3\frac{\partial}{\partial t}\left(\frac{\partial u}{\partial y}+\frac{\partial v}{\partial x}\right)+a_4\frac{\partial u_a}{\partial t}+a_5\frac{\partial u_{\mathrm{w}}}{\partial t}=\frac{k_w}{r_w}\left\{\frac{\partial}{\partial x}\left[\frac{\partial u_{\mathrm{w}}}{\partial x}\right]+\frac{\partial}{\partial y}\left[\frac{\partial}{\partial y}(u_{\mathrm{w}}+y)\right]\right\}-q_{\mathrm{w}} \tag{41}$$

$$b_1\frac{\partial}{\partial t}\frac{\partial u}{\partial x}+b_2\frac{\partial}{\partial t}\frac{\partial v}{\partial y}b_3+a_3\frac{\partial}{\partial t}\left(\frac{\partial u}{\partial y}+\frac{\partial v}{\partial x}\right)+b_4\frac{\partial u_{\mathrm{a}}}{\partial t}+b_5\frac{\partial u_{\mathrm{w}}}{\partial t}=\frac{k_a}{r_w}\left\{\frac{\partial}{\partial x}\left[\frac{\partial u_{\mathrm{a}}}{\partial x}\right]+\frac{\partial}{\partial y}\left[\frac{\partial u_{\mathrm{a}}}{\partial y}\right]\right\}-q_{\mathrm{a}} \tag{42}$$

where A_i, F_i, and D_{ij} (i, j = 1, 2, 3, 4, 5, and 6) are the matrix element signs as given in a previous study [31]. In addition, a_i and b_i (i = 1, 2, 3, 4, 5, and 6) are given by Eqs. (43)–(51), respectively.

$$a_1=\frac{D_{11}+D_{21}+D_{31}}{3K_{\mathrm{wpt}}}+ns_r+\frac{A_1D_{11}+A_2D_{21}+A_3D_{31}+A_4D_{41}+A_5D_{51}+A_6D_{61}}{K_{\mathrm{wqt}}} \tag{43}$$

$$a_2=\frac{D_{12}+D_{22}+D_{32}}{3K_{\mathrm{wpt}}}+ns_r+\frac{A_1D_{12}+A_2D_{22}+A_3D_{32}+A_4D_{42}+A_5D_{52}+A_6D_{62}}{K_{\mathrm{wqt}}} \tag{44}$$

$$a_3 = \frac{D_{14} + D_{24} + D_{34}}{3K_{\mathrm{wpt}}} + \frac{A_1D_{12} + A_2D_{22} + A_3D_{32} + A_4D_{42} + A_5D_{52} + A_6D_{62}}{K_{\mathrm{wqt}}} \tag{45}$$

$$a_4 = -a_5 = -\left(\frac{F_1 + F_2 + F_3}{3K_{\mathrm{wpt}}} + \frac{1}{H_{\mathrm{wt}}} + \frac{A_1F_1 + A_2F_2 + A_3F_3 + A_4F_4 + A_5F_5 + A_6F_6}{K_{\mathrm{wqt}}}\right) \tag{46}$$

$$b_1 = 1 - a_1 \tag{47}$$

$$b_2 = 1 - a_2 \tag{48}$$

$$b_3 = -a_3 \tag{49}$$

$$b_4 = a_4 + (n - \theta)/P_g \tag{50}$$

$$b_5 = -a_5 \tag{51}$$

From the above analysis, we can see that Eqs. (39)–(42) are the governing equations of the new EDSCM of unsaturated undisturbed loess in plane coordinate.

3.3 Discretization of governing equations

The governing equations (Eqs. 39–42) of EDSCM have been discretized using the Galerkin method. As the weighting function in the Galerkin method is the same as the shape function, the governing equations (Eqs. 39–42) can be obtained by the weighted integration method, which has two domains: One is the space domain, and the other is the time domain. Assuming that the shape function of the displacement is the same as that of the pore pressure, the element displacement and pore pressure can be expressed as follows:

$$u = N_j u_j, \quad v = N_j v_j, \quad u_a = N_j u_{aj}, \quad u_w = N_j u_{wj} \tag{52}$$

where N_j is the shape function which is the same as N_i, and j = 1, 2, 3, and 4.

The shape function of the quadrilateral isoparametric element in the plane coordinate can be written as:

$$N_i = \frac{(1 + \xi_i\xi)(1 + \eta_i\eta)}{4} \quad i = 1,2,3,4 \tag{53}$$

where ξ and η are the local coordinates, i.e., $\xi_1 = -1$, $\eta_1 = -1$; $\xi_2 = 1$, $\eta_2 = -1$; $\xi_3 = 1$, $\eta_3 = 1$; and $\xi_4 = -1$, $\eta_4 = 1$.

By combining Eq. (39) and Eq. (40) with the Green formula in the space domain, we obtain:

$$\begin{aligned}
&\iint_A u_j\left(D_{11}\frac{\partial N_i}{\partial x}\frac{\partial N_j}{\partial x} + D_{14}\frac{\partial N_i}{\partial x}\frac{\partial N_j}{\partial y} + D_{41}\frac{\partial N_i}{\partial x}\frac{\partial N_j}{\partial y} + D_{44}\frac{\partial N_i}{\partial y}\frac{\partial N_j}{\partial y}\right)\mathrm{d}x\mathrm{d}y \\
&+ \iint_A v_j\left(D_{12}\frac{\partial N_i}{\partial x}\frac{\partial N_j}{\partial y} + D_{14}\frac{\partial N_i}{\partial x}\frac{\partial N_j}{\partial x} + D_{42}\frac{\partial N_i}{\partial y}\frac{\partial N_j}{\partial y} + D_{44}\frac{\partial N_i}{\partial y}\frac{\partial N_j}{\partial x}\right)\mathrm{d}x\mathrm{d}y \\
&- \iint_A u_{aj}\left[(F_1 + 1)N_j\frac{\partial N_i}{\partial x} - F_4N_j\frac{\partial N_i}{\partial y}\right]\mathrm{d}x\mathrm{d}y \\
&+ \iint_A u_{wj}\left(F_1N_j\frac{\partial N_i}{\partial x} - F_4N_j\frac{\partial N_i}{\partial y}\right)\mathrm{d}x\mathrm{d}y = F_{i1}
\end{aligned} \tag{54}$$

$$\begin{aligned}
&\iint_A u_j\left(D_{21}\frac{\partial N_i}{\partial x}\frac{\partial N_j}{\partial y} + D_{24}\frac{\partial N_i}{\partial y}\frac{\partial N_j}{\partial y} + D_{41}\frac{\partial N_i}{\partial x}\frac{\partial N_j}{\partial x} + D_{44}\frac{\partial N_i}{\partial x}\frac{\partial N_j}{\partial y}\right)\mathrm{d}x\mathrm{d}y \\
&+ \iint_A v_j\left(D_{22}\frac{\partial N_i}{\partial y}\frac{\partial N_j}{\partial y} + D_{24}\frac{\partial N_i}{\partial y}\frac{\partial N_j}{\partial x} + D_{42}\frac{\partial N_i}{\partial y}\frac{\partial N_j}{\partial x} + D_{44}\frac{\partial N_i}{\partial x}\frac{\partial N_j}{\partial x}\right)\mathrm{d}x\mathrm{d}y \\
&- \iint_A u_{aj}\left[F_4N_j\frac{\partial N_i}{\partial x} + (F_2 + 1)_4N_j\frac{\partial N_i}{\partial y}\right]\mathrm{d}x\mathrm{d}y \\
&+ \iint_A u_{wj}\left(F_4N_j\frac{\partial N_i}{\partial x} + F_2N_j\frac{\partial N_i}{\partial y}\right)\mathrm{d}x\mathrm{d}y = F_{i2}
\end{aligned} \tag{55}$$

For the integral method in the time domain, the integral equation from t to $(t + \Delta t)$ is as follows:

$$\int_t^{t+\Delta t} f(t)\mathrm{d}t = \xi f(t + \Delta t) + (1 - \xi)f(t) \tag{56}$$

where Δt is time step. ξ is time integral parameter. $f(t + \Delta t)$ and $f(t)$ are the functions relating to $(t + \Delta t)$ and t, respectively. Based on the results from the earlier literature [6], when $\xi \geq 1/2$, the solution of Eq. (56) can be obtained. In this paper, ξ = 2/3. Using Eq. (56), the governing equations in the time domain can then be discretized.

Similarly, combining Eqs. (41) and (42) with the Green formula and integrating them by t $(t_1 \leq t \leq t_2)$ give the expressions for the displacement and the pore pressure, respectively:

$$\iint_A N_i\left\{\left(a_1\frac{\partial N_j}{\partial x}+a_3\frac{\partial N_j}{\partial y}\right)u_j^{(2)}+\left(a_2\frac{\partial N_j}{\partial y}+a_3\frac{\partial N_j}{\partial x}\right)v_j^{(2)} + a_4N_ju_{aj}^{(2)}+\left[a_5N_j+\frac{k_w}{r_w}\left(\frac{\partial N_i}{\partial x}\frac{\partial N_j}{\partial x}+\frac{\partial N_i}{\partial y}\frac{\partial N_j}{\partial y}\right)\xi\Delta t\right]u_{wj}^{(2)}\right\} \mathrm{d}x\mathrm{d}y = F_{i3} \tag{57}$$

$$\iint_A N_i\left\{\left(b_1\frac{\partial N_j}{\partial x}+b_3\frac{\partial N_j}{\partial y}\right)u_j^{(2)}+\left(b_2\frac{\partial N_j}{\partial y}+b_3\frac{\partial N_j}{\partial x}\right)v_j^{(2)} +b_5N_ju_{wj}^{(2)}+\left[b_4N_iN_j+\frac{k_a}{r_w}\left(\frac{\partial N_i}{\partial x}\frac{\partial N_j}{\partial x}+\frac{\partial N_i}{\partial y}\frac{\partial N_j}{\partial y}\right)\xi\Delta t\right] \cdot u_{aj}^{(2)}\right\}\mathrm{d}x\mathrm{d}y = F_{i4} \tag{58}$$

Through the above simplifications (Eqs. 54–55 and 57–58) in the space and time domain, the expressions of the loading terms F_{i1}, F_{i2}, F_{i3} and F_{i4} are as follows:

$$\begin{aligned}F_{i1} = {} & \oint D_{11}N_i\frac{\partial u}{\partial x}\mathrm{d}y-\oint D_{12}N_i\frac{\partial v}{\partial y}\mathrm{d}y \\ & +\oint D_{14}N_i\left(\frac{\partial v}{\partial x}+\frac{\partial u}{\partial y}\right)\mathrm{d}y \\ & +\oint D_{41}N_i\frac{\partial u}{\partial y}\mathrm{d}y-\oint D_{42}N_i\frac{\partial v}{\partial y}\mathrm{d}x \\ & -\oint D_{44}N_i\left(\frac{\partial u}{\partial y}+\frac{\partial v}{\partial x}\right)\mathrm{d}x \\ & -\oint N_i(F_1+1)u_{\mathrm{a}}\mathrm{d}y+\oint N_iF_4u_{\mathrm{a}}\mathrm{d}x \\ & +\oint N_iF_1u_{\mathrm{w}}\mathrm{d}y-\oint N_iF_4u_{\mathrm{w}}\mathrm{d}x-\iint_A N_if_{0x}\mathrm{d}x\mathrm{d}y\end{aligned} \tag{59}$$

$$\begin{aligned}F_{i2} = {} & D_{41}\oint N_i\frac{\partial u}{\partial x}\mathrm{d}y-D_{42}\oint N_i\frac{\partial v}{\partial x}\mathrm{d}x \\ & +D_{44}\oint N_i\left(\frac{\partial v}{\partial x}+\frac{\partial u}{\partial y}\right)\mathrm{d}y \\ & +D_{21}\oint N_i\frac{\partial u}{\partial y}\mathrm{d}y-D_{22}\oint N_i\frac{\partial v}{\partial y}\mathrm{d}x \\ & -D_{24}\oint N_i\left(\frac{\partial v}{\partial x}+\frac{\partial u}{\partial y}\right)\mathrm{d}x \\ & -\oint N_iF_4u_{\mathrm{a}}\mathrm{d}y+\oint N_i(F_2+1)u_{\mathrm{a}}\mathrm{d}x+\oint N_iF_4u_{\mathrm{w}}\mathrm{d}y \\ & -\oint N_iF_2u_{\mathrm{w}}\mathrm{d}x-\iint_A N_if_{0y}\mathrm{d}x\mathrm{d}y\end{aligned} \tag{60}$$

$$\begin{aligned}F_{i3} = {} & \frac{k_{\mathrm{w}}}{r_{\mathrm{w}}}\int_t^{\Delta t}\left(\oint N_i\frac{\partial u_{\mathrm{w}}}{\partial x}\mathrm{d}y-\oint N_i\frac{\partial u_w}{\partial y}\mathrm{d}x\right)\mathrm{d}t \\ & -\frac{k_{\mathrm{w}}\Delta t}{r_{\mathrm{w}}}\iint_A\frac{\partial N_i}{\partial y}\mathrm{d}x\mathrm{d}y \\ & +\sum_{J=1}^{4}\left\{K_{ij}^{31}u_j^t+K_{ij}^{32}v_j^t+K_{ij}^{33}u_{aj}^t \right. \\ & \left.+\left[K_{ij}^{34}-\iint_A\frac{k_{\mathrm{w}}\Delta t}{r_{\mathrm{w}}}\left(\frac{\partial N_i}{\partial x}\frac{\partial N_j}{\partial x}+\frac{\partial N_i}{\partial y}\frac{\partial N_j}{\partial y}\right)\mathrm{d}x\mathrm{d}y\right]\cdot u_{\mathrm{w}j}^t\right\} \\ & +q_{\mathrm{w}}\Delta t\iint_A\frac{\partial N_i}{\partial y}\mathrm{d}x\mathrm{d}y,\end{aligned} \tag{61}$$

$$\begin{aligned}F_{i4} = {} & \frac{k_{\mathrm{a}}}{r_{\mathrm{w}}}\left(\oint N_i\frac{\partial N_ju_{\mathrm{a}j}}{\partial x}\mathrm{d}x-\oint N_i\frac{\partial N_ju_{\mathrm{a}j}}{\partial y}\mathrm{d}y\right) \\ & +\sum_{J=1}^{4}\left\{K_{ij}^{41}u_j^t+K_{ij}^{42}v_j^t+K_{ij}^{44}u_{\mathrm{w}j}^t \right. \\ & \left.+\left[K_{ij}^{43}-\iint_A\frac{k_{\mathrm{a}}\Delta t}{r_{\mathrm{w}}}\left(\frac{\partial N_i}{\partial x}\frac{\partial N_j}{\partial x}+\frac{\partial N_i}{\partial y}\frac{\partial N_j}{\partial y}\right)\mathrm{d}x\mathrm{d}y\right]\cdot u_{\mathrm{a}j}^t\right\} \\ & +q_a\Delta t\iint_A\frac{\partial N_i}{\partial y}\mathrm{d}x\mathrm{d}y.\end{aligned} \tag{62}$$

3.4 Specific expression of matrix elements

The finite element equations for solving plane problems can be derived from the specific forms of the governing equations:

$$\sum_{e=1}^{MELES}\sum_{j=1}^{NNODE}\left[K_{ij}\right]_e^{t+\Delta t}\{X_i\}_e^{t+\Delta t}=\sum_{e=1}^{MELES}\{R_i\}_e^{t+\Delta t} \tag{63}$$

where *MELES* is the total number of structural units, i = 1, 2, 3, 4…*MELES*. *NNODE* is the number of unit node. In this paper, we used the 4-node isoparametric element. Therefore, *NNODE* = 4. $\{\boldsymbol{X}_i\}_{\mathrm{e}}^{t+\Delta t}$ is the displacement vector. $\{\boldsymbol{R}_i\}_{\mathrm{e}}^{t+\Delta t}$ is the load vector.

The modulus matrix of the element is a 16 × 16 matrix, and therefore, each rigid sub-block is a 4 × 4 matrix. The expressions of 16 elements are as follows:

$$\left[K_{ij}\right]_e^{t+\Delta t}=\begin{bmatrix}K_{ij}^{11} & K_{ij}^{12} & K_{ij}^{13} & K_{ij}^{14}\\ K_{ij}^{21} & K_{ij}^{22} & K_{ij}^{23} & K_{ij}^{24}\\ K_{ij}^{31} & K_{ij}^{32} & K_{ij}^{33} & K_{ij}^{34}\\ K_{ij}^{41} & K_{ij}^{42} & K_{ij}^{43} & K_{ij}^{44}\end{bmatrix}_e^{t+\Delta t} \tag{64}$$

The concrete expressions for the modulus matrix

elements in the above equation are written as the following functions:

$$K_{ij}^{11} = \iint_A \left[D_{11}\frac{\partial N_i}{\partial x}\frac{\partial N_j}{\partial x} + D_{14}\frac{\partial N_i}{\partial x}\frac{\partial N_j}{\partial y} + D_{41}\frac{\partial N_i}{\partial x}\frac{\partial N_j}{\partial y} + D_{44}\frac{\partial N_i}{\partial y}\frac{\partial N_j}{\partial y}\right] \mathrm{d}x\mathrm{d}y \tag{65}$$

$$K_{ij}^{12} = \iint_A \left[D_{12}\frac{\partial N_i}{\partial x}\frac{\partial N_j}{\partial y} + D_{14}\frac{\partial N_i}{\partial x}\frac{\partial N_j}{\partial x} + D_{42}\frac{\partial N_i}{\partial y}\frac{\partial N_j}{\partial y} + D_{44}\frac{\partial N_i}{\partial y}\frac{\partial N_j}{\partial x}\right] \mathrm{d}x\mathrm{d}y \tag{66}$$

$$K_{ij}^{13} = -\iint_A \left[(F_1+1)N_j\frac{\partial N_i}{\partial x} - F_4 N_j\frac{\partial N_i}{\partial y}\right] \mathrm{d}x\mathrm{d}y \tag{67}$$

$$K_{ij}^{14} = \iint_A \left[F_1 N_j\frac{\partial N_i}{\partial x} - F_4 N_j\frac{\partial N_i}{\partial y}\right] \mathrm{d}x\mathrm{d}y \tag{68}$$

$$K_{ij}^{21} = \iint_A \left[D_{21}\frac{\partial N_i}{\partial x}\frac{\partial N_j}{\partial y} + D_{24}\frac{\partial N_i}{\partial y}\frac{\partial N_j}{\partial y} + D_{41}\frac{\partial N_i}{\partial x}\frac{\partial N_j}{\partial x} + D_{44}\frac{\partial N_i}{\partial x}\frac{\partial N_j}{\partial y}\right] \mathrm{d}x\mathrm{d}y \tag{69}$$

$$K_{ij}^{22} = \iint_A \left[D_{22}\frac{\partial N_i}{\partial y}\frac{\partial N_j}{\partial y} + D_{24}\frac{\partial N_i}{\partial y}\frac{\partial N_j}{\partial x} + D_{42}\frac{\partial N_i}{\partial y}\frac{\partial N_j}{\partial x} + D_{44}\frac{\partial N_i}{\partial x}\frac{\partial N_j}{\partial x}\right] \mathrm{d}x\mathrm{d}y \tag{70}$$

$$K_{ij}^{23} = -\iint_A u_{aj}\left[F_4 N_j\frac{\partial N_i}{\partial x} + (F_2+1)N_j\frac{\partial N_i}{\partial y}\right] \mathrm{d}x\mathrm{d}y \tag{71}$$

$$K_{ij}^{24} = \iint_A u_{wj}\left(F_4 N_j\frac{\partial N_i}{\partial x} + F_2 N_j\frac{\partial N_i}{\partial y}\right) \mathrm{d}x\mathrm{d}y \tag{72}$$

$$K_{ij}^{31} = \iint_A N_i\left(a_1\frac{\partial N_j}{\partial x} + a_3\frac{\partial N_j}{\partial y}\right) \mathrm{d}x\mathrm{d}y \tag{73}$$

$$K_{ij}^{32} = \iint_A N_i\left(a_2\frac{\partial N_j}{\partial y} + a_3\frac{\partial N_j}{\partial x}\right) \mathrm{d}x\mathrm{d}y \tag{74}$$

$$K_{ij}^{33} = \iint_A N_i a_4 N_j \mathrm{d}x\mathrm{d}y \tag{75}$$

$$K_{ij}^{34} = \iint_A \left[a_5 N_i N_j + \frac{k_w}{r_w}\left(\frac{\partial N_i}{\partial x}\frac{\partial N_j}{\partial x} + \frac{\partial N_i}{\partial y}\frac{\partial N_j}{\partial y}\right)\xi\Delta t\right] \mathrm{d}x\mathrm{d}y \tag{76}$$

$$K_{ij}^{41} = \iint_A N_i\left(b_1\frac{\partial N_j}{\partial x} + b_3\frac{\partial N_j}{\partial y}\right) \mathrm{d}x\mathrm{d}y \tag{77}$$

$$K_{ij}^{42} = \iint_A N_i\left(b_2\frac{\partial N_j}{\partial y} + b_3\frac{\partial N_j}{\partial x}\right) \mathrm{d}x\mathrm{d}y \tag{78}$$

$$K_{ij}^{43} = \iint_A \left[b_4 N_i N_j + \frac{k_a}{r_w}\left(\frac{\partial N_i}{\partial x}\frac{\partial N_j}{\partial x} + \frac{\partial N_i}{\partial y}\frac{\partial N_j}{\partial y}\right)\xi\Delta t\right] \mathrm{d}x\mathrm{d}y \tag{79}$$

$$K_{ij}^{44} = \iint_A N_i b_5 N_j \mathrm{d}x\mathrm{d}y \tag{80}$$

Further, the final forms of the consolidation control equations have been obtained through the discretizations of the space and time domains. As part of the discretizing process, if the displacement and pore pressure of each node are known at time t, the corresponding displacement and pore pressure at time $(t + \Delta t)$ can then be determined. The total stiffness matrix has been transformed into a new matrix which is only left over by the complete Gauss elimination method. According to the load terms F_{i1} and F_{i2}, and the boundary flows F_{i3} and F_{i4}, the finite element analysis of seepage consolidation coupling problem can be carried out under the loading and soaking actions.

4 Numerical simulations and results

4.1 The modeled domain

Based on the new EDSCM of unsaturated undisturbed loess and drawing on the results reported in some of the well-known studies [3, 6, 22], a corresponding finite element program termed as ULEDSC has been compiled. The ULEDSC uses a four-node isoparametric element, which consists of two main procedures and twenty-six sub-procedures. The detailed procedure has been described in a previous study [31]. In order to effectively compare the field monitoring results with the illustrative numerical simulations, the large-scale field-soaking test of self-weight

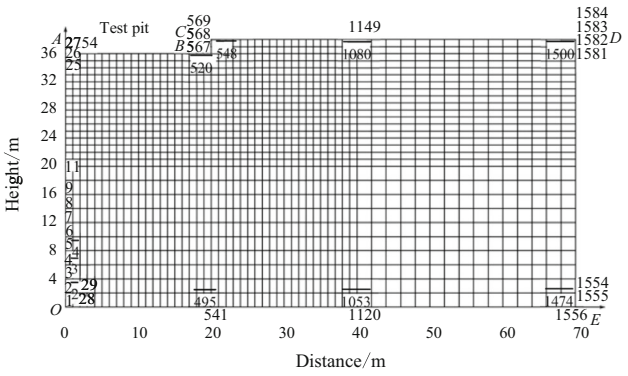

Fig. 1 Two-dimensional mesh (of 1500 elements) of the modeled domain (unit: m)

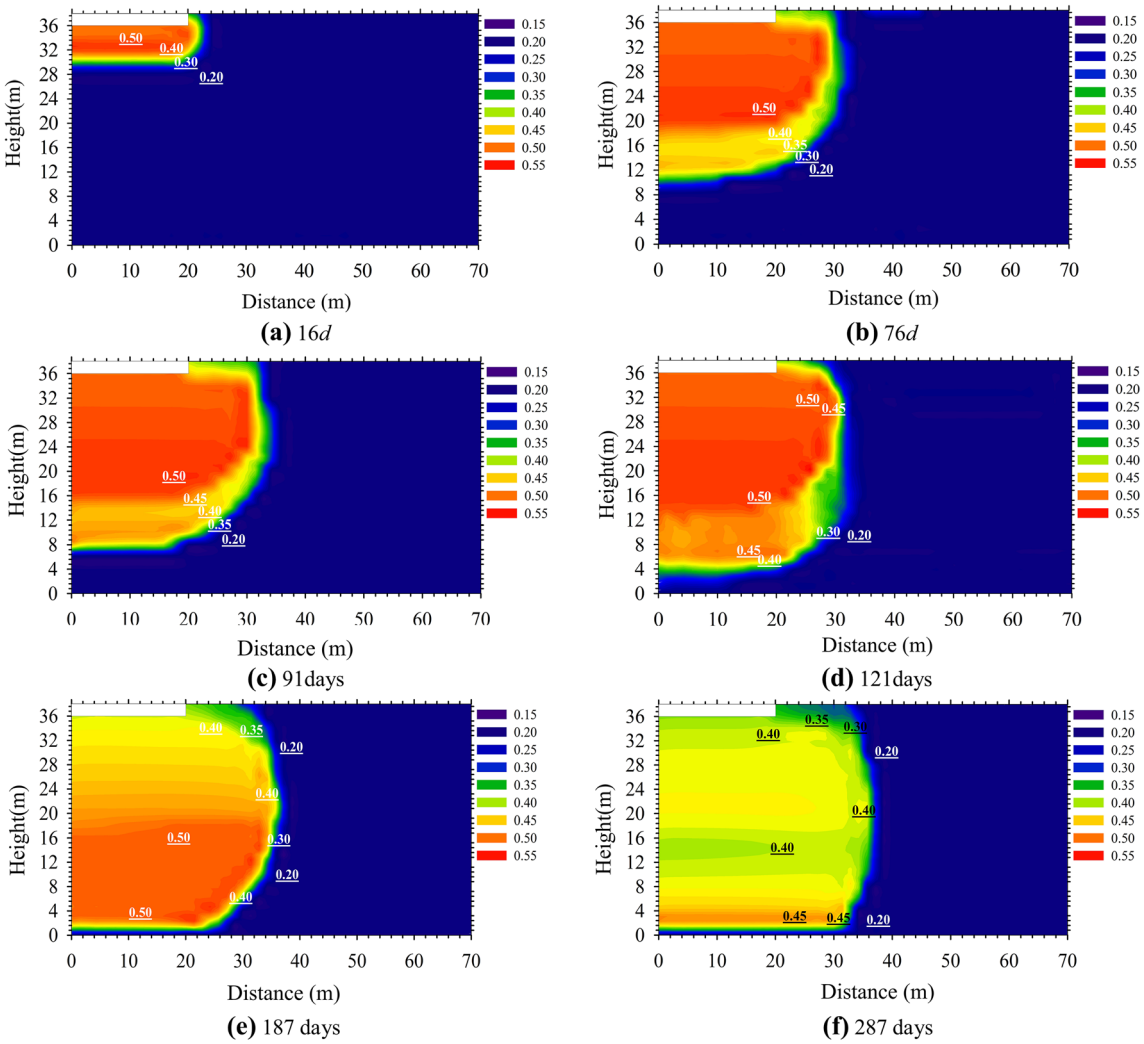

Fig. 2 Contours of volumetric water content at different days

collapsible loess located at Heping town, Lanzhou city, Gansu Province in China, has been used as the example. The thickness of collapsible soil layer in the studied area exceeds 36.5 m.

The infiltration process is adequately represented on the x–z plane (where x and z are the horizontal and vertical axes, respectively). Furthermore, no changes were assumed along the y axis. The radius of the test pit is the same as that of the field test and is 20 m. The two-dimensional simulation domain was 70 m in the horizontal direction and 38 m in the vertical direction. The height of the test pit is 2 m. In this paper, only half of the field test has been used to simulate its wetting and subsequent drying periods. This numerical domain has been discretized into 1500 quadrilateral elements and 1584 nodes. $\bar{1} - \overline{1500}$ represents the quadrilateral elements, and 1–1581 represents the node number in Fig. 1. The sizes of elements are 1 m (width) × 2 m (length), 2 m (width) × 1 m (length), and 2 m (width) × 2 m (length), respectively.

The six corner points are designated as A, B, C, D, E, and O, as shown in Fig. 1. The bottom OE of the numerical domain has been assumed to be under a unit gradient condition. Except for the center zone corresponding to the infiltrating test pit of the domain, the left side OA, right side DE, and the top surfaces BC and CD have been assumed to be the impermeable boundaries. A constant head boundary of 0.5 m was assumed for the base of the test pit of the top boundary AB, which reflects the pond head. The initial dry density, initial suction, initial volume water content, void ratio, yield suction, yield stress, and initial pore pressure of the whole site are 1.35 g/cm^3, 250 kPa, 0.20, 1.01, 120 kPa, 140 kPa, and 0 kPa, respectively.

4.2 Wetting and drying simulations

There are two parts in the numerical analysis, i.e., an initial 151-day period of wetting and a subsequent 251-day period of drying. For the entire infiltrating area and different time

periods, the multi-field coupling calculations corresponding to the moisture field (volumetric water content), pore pressure field (pore water pressure and air pressure), displacement field (horizontal displacement and vertical displacement), and damage field have been carried out. Depending on the calculation requirement, different time steps have been used for different time periods.

Figure 2a and b shows the variations of the volumetric water content at 91 and 121 days during the initial wetting period. It can be seen that the shape of the wetting front is similar to that of a semi-elliptical. Because the modeled domain is symmetrical, the propagation of the wetting front is identical to a pumpkin-shaped zone. This result is identical to those of Huang et al. [17] and Gvirtzman et al. [13] and is also identical to that experimentally reported in a previous study [35]. These results described by Yao et al. [35] can be compared with the numerical simulations of this study. In Fig. 2a, the wetting front in horizontal direction is 13 m from the edge of the test pit, and the vertical migration distance is 30 m to the center of the test pit after 91 days. In the field test, the horizontal migration was 13 m, and the vertical migration was 27.5 m after 93 days [23]. In Fig. 2b, the wetting front in horizontal direction is 14 m from the edge of the test pit, and the vertical migration distance is 34 m to the center of the test pit after 121 days. In the field test [35], the horizontal migration was 13 m, and the vertical migration was 32.5 m after 121 days. Hence, for the shorter wetting period, the simulated values are in accordance with the measured values.

Figure 2c and d shows the variations of the volumetric water content at 187 and 287 days during the subsequent drying period. Comparing with volumetric water contents in Fig. 2a and b, the saturation areas are bigger and extending to the bottom of the model. However, the volumetric water content below the bottom of the test pit decreases from 0.50 cm^3/cm^3 (Fig. 2a, b) to 0.45 cm^3/cm^3 (Fig. 2c, d). This is an indication that the water in saturated loess flows slowly downward from the test pit with no external water supply, which makes the original saturated loess gradually transit to unsaturated state. This trend is more clearly shown in Fig. 2d. During the initial wetting stage, the loess near the bottom of the test pit is transformed to a saturated state. During the subsequent drying stage, it is then gradually transformed from the saturated to the unsaturated state with decreasing volumetric water content and dehydration.

At the test site, the self-weight collapsible loess after going through the wetting and the subsequent drying produces large deformations which include the horizontal and vertical displacements. The vertical displacement deformation is mainly the result of the collapsible deformation during the wetting stage and the consolidation deformation during the subsequent drying stage. With water infiltrating slowly, the loess collapses and the vertical displacement occurs due to the self-weight and water. According to the vertical displacement shown in Fig. 3, the vertical displacement diagrams are identical to those of the volumetric

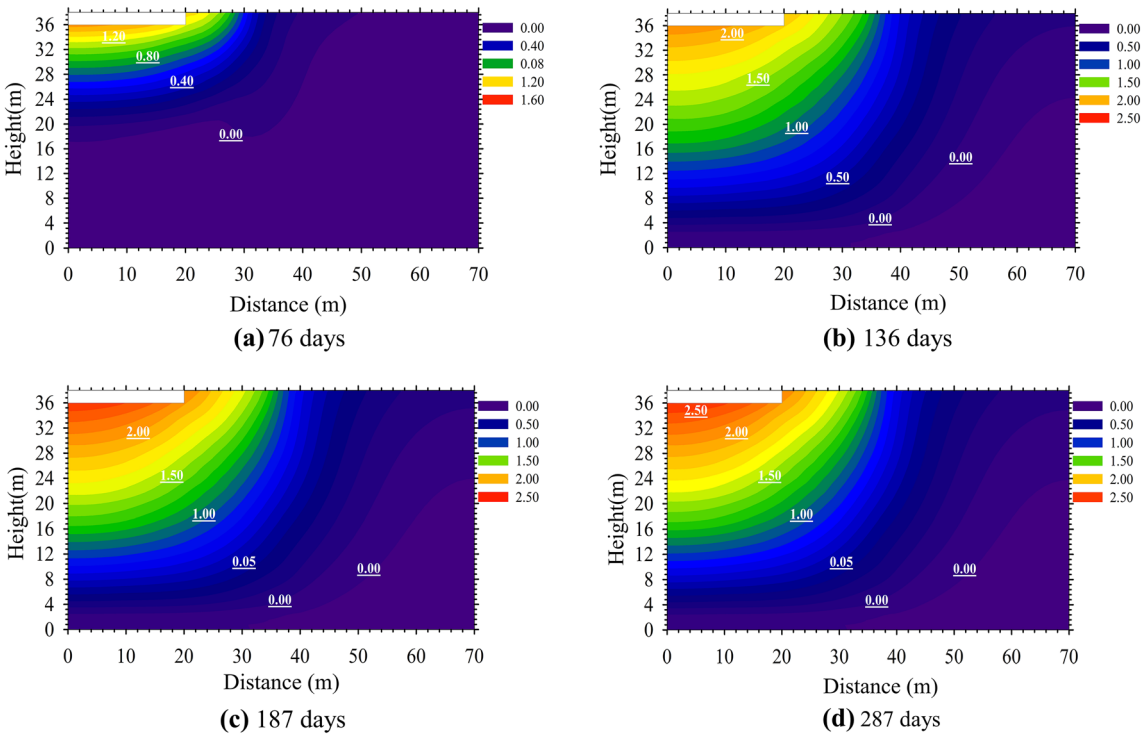

Fig. 3 Contours of vertical displacement at different days

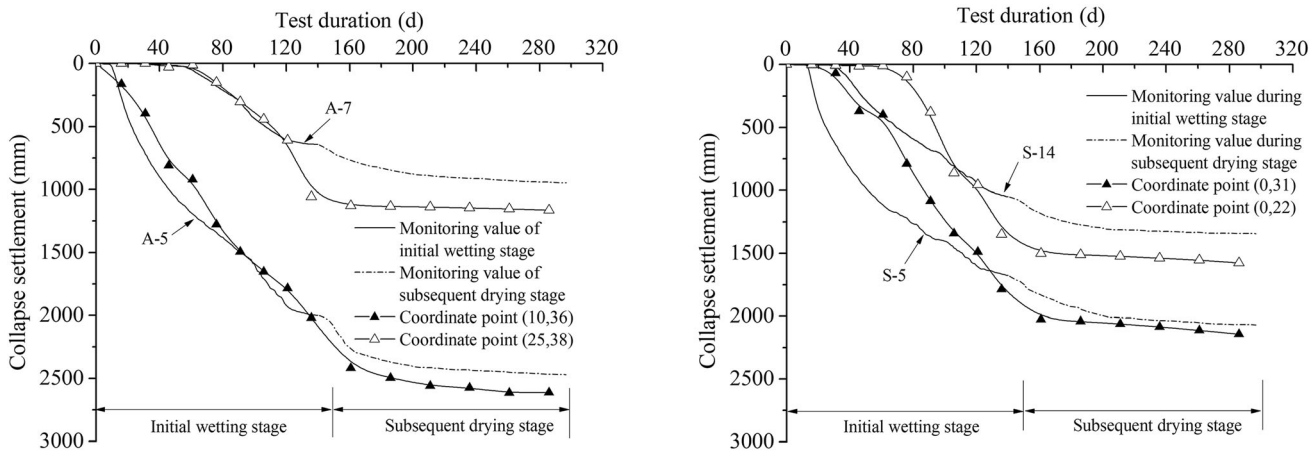

(a) Surface observation points **(b)** Deep observation points

Fig. 4 Comparison of measured and simulated collapse settlement at surface and deep observation points. Coordinate point (10, 36) corresponds to 10 m in the horizontal direction and 36 m in the vertical direction, as shown in Fig. 2. The coordinate points (25, 38), (0, 31), and (0, 22) carry similar meanings. A-5 and A-7 represent the distances of 5 m and 7 m from the surface observation Point A in the horizontal direction, respectively. S-5 and S-14 show the distances of 5 m and 14 m from the base of the test pit of top boundary AB, as shown in Fig. 1, respectively

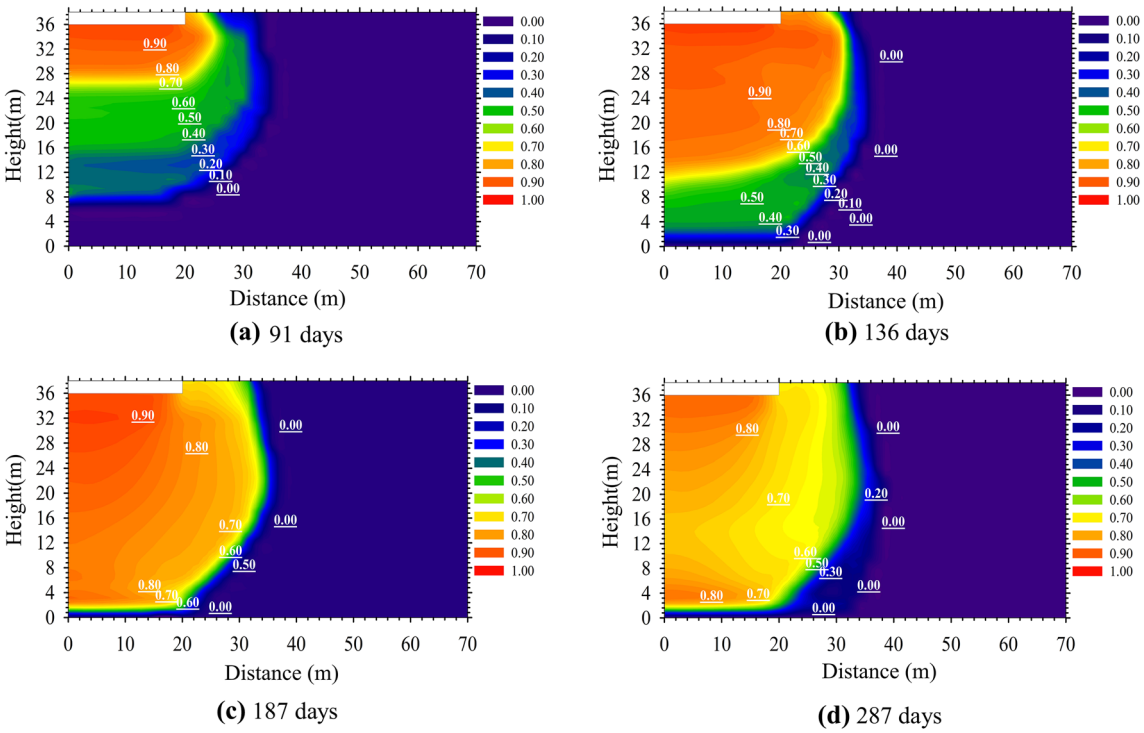

(a) 91 days **(b)** 136 days

(c) 187 days **(d)** 287 days

Fig. 5 Contours of damage evolution at different days

water content (Fig. 2), but the infiltrating ranges are greater than those of volumetric water content in Fig. 2a and b.

Figure 3c and d shows parts of the vertical displacements during the subsequent drying stage. It can be seen that the variation of the vertical displacement is small, the final vertical displacement during the initial wetting stage (Fig. 3b) is about 1.98 m, and the final vertical displacement during the subsequent drying stage (Fig. 3d) is 2.43 m. So, the final vertical displacement during the drying stage is only 0.45 m. The vertical displacement during the subsequent drying stage is mainly caused by the loess collapse and consolidation settlements. Further, the consolidation settlements mainly occur at the bottom layer of the saturated loess. Hence, the collapsible deformation mainly occurs at the deeper foundation below the test pit. However, the collapsible deformation just beneath the test

pit is relatively smaller. So, the vertical displacement during subsequent drying stage is mainly caused by the consolidation settlements of the shallow soil layer just under the test pit.

The vertical displacement of each node in the modeled domain has been determined. These simulated displacements can be compared with that measured by Yao et al. [23] with the surface and deep observation points. Taking the coordinate points (10, 36), (25, 38), (0, 31), and (0, 22) as an example (Fig. 1), the four coordinate points correspond to Curves A-5, A-7, S-5, and S-14 [23]. Figure 4 shows comparisons of the measured and simulated collapse settlements at surface and deep observation points. From Fig. 4a during the initial wetting stage, it can be seen that the simulated settlements at the surface observation point A-5 are slightly larger than the measured settlements at point (10, 36). On the other hand, the simulated settlements at the surface observation point A-7 are in accordance with the measured settlements during the wetting period and are greater than those during the drying stage. For the deep settlement observation points S-5 and S-14, there are differences between the simulated and measured settlements.

Based on the simulated displacement increment and volumetric water content change during the wetting and subsequent drying periods, the collapsible volumetric strain and the collapsible deviatoric strain can be determined. By substituting the volumetric and deviatoric strain into the structural damage evolution equation, the damage of each node can be obtained. Figure 5 shows the partial damage evolution pictures. It can be seen that the longer the test period, the larger the damage area. Further, the damage area is identical to that of the wetting front, which reflects the effect of water on the structural damage. Due to the definition of damage, the occurrence of damage is closely related to the deformation and volumetric water content. According to the damage value between 0–0.3, 0.3–0.7, and 0.7–1, the area with water immersion deformation can be divided into three parts, i.e., mild damage, moderate damage, and severe damage. This is similar to the three parts of the wetting zone shown in Fig. 2, i.e., saturation zone, conduction zone, and wetting zone. In addition, from the top pit to bottom pit of the modeled domain, the loess collapsibility gradually decreases.

In addition, Fig. 5c and d shows that the damage of the infiltration zone between the bottom of the test pit and the lower boundary of the modeled domain is greater during the drying period, but the damages in the middle and lateral of the infiltrated area are smaller. Although the collapsible deformation is smaller during this period, the volumetric water content at the bottom of the model is practically saturated. Therefore, these two parts of the collapsible deformation and volumetric water content govern the overall damage. In the middle part of the infiltration zone and near the wetting front region, the damage is smaller due to the lower volumetric water content and smaller collapsible deformation, and its change rule is different from the damage evolution during initial wetting periods.

5 Discussion

5.1 Morphology of wetting front

From the field-soaking tests [35] and the numerical results published in a previous work (as shown in Fig. 2), it was found that the morphology of wetting front was similar to elliptic infiltration. Some research results show that the water transport pattern of the self-weight collapsible loess site is similar to that of the inverted bowl type, which was more prominent in the soaking tests along the Zheng-Xi high-speed railway line [23]. However, some results were in accordance with those reported in the current paper. There were no pre-injection holes in the self-weight collapsible loess soaking test site of Chuanda expressway [30]. A large number of observations from the TDR moisture meter showed that the moisture morphology was similar to that of the on-site monitoring [35], which was in elliptical state. Huang et al. [17] showed that the water infiltrated in the entire soil layer was similar to an ellipse (in shape) in the slope soaking experiment.

In addition, Gvirtzman et al. [13] conducted two soaking water experiments on two sandy loess sites. The TDR moisture meter showed that part of the immersed water was in the form of an ellipse, while the other was onion-shaped. Furthermore, the morphology of wetting front obtained using numerical calculations presented an elliptical shape. This is similar to the results of numerical experiments conducted in this paper. The final form of water immersion is closely related to the geological environment, and the related results still need to be further studied.

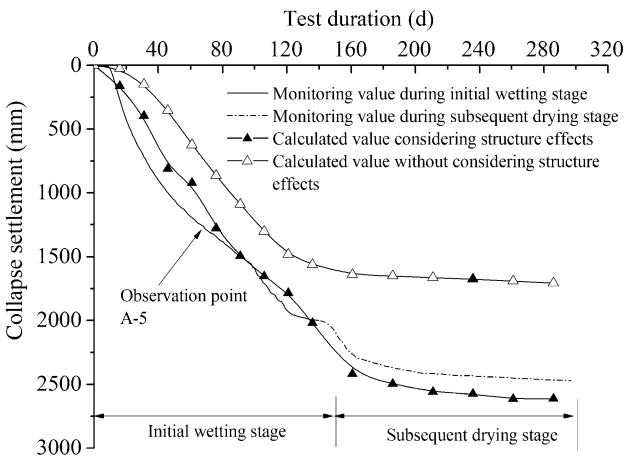

Fig. 6 Effect of structural damage on the collapse deformation

The results showed that the water transfer in the area of self-weight collapsible loess presented the elliptical morphology for infiltration at the early wetting stage and became irregular at the subsequent drying stage. Furthermore, large collapse deformation occurred in the upper loess. On the one hand, the upper loess has already produced large collapsible deformation, and the increase in density hinders further migration of water. The gas resistance effect formed by excess gas in the process of water infiltration cannot be excluded, which affects the migration of water. On the other hand, the lower permeability coefficient of unsaturated soil affected the infiltration, whereas the unsaturated permeability coefficient gradually increased with the increase in the degree of saturation. It is found through actual measurements that the degree of saturation lay within the range of 0.4–0.6. The unsaturated permeability coefficient corresponding to the degree of saturation of 0.4 was two orders of magnitude lower than the value corresponding to the degree of saturation of 0.6 [31]. Therefore, when the original site was not saturated, the lower unsaturated permeability coefficient further impeded the water infiltration. Gvirtzman et al. [13] also obtained similar results using experimental and numerical techniques.

5.2 Structural damage to the deformation

Taking coordinate point (20,36) as the calculation object corresponding to the observation point A-5, the vertical displacement under two working conditions with/without considering structural damage is calculated. The results obtained from the calculations are shown in Fig. 6. It can be seen that the vertical displacement values with considering the structural damage were in accordance with the actual situation. However, the vertical displacement values without considering the structural damage were relatively small and were due to the increase in the deformation values caused by the structural damage. Moreover, the increasing deformation values had a cumulative effect and became more obvious in the subsequent drying stages. It can be concluded that the structural damage could reflect the softening of structure when it was soaked. In addition, the structural damage can increase the collapse deformation, which made a significant contribution to simulate the collapsible deformation.

It should be noted that in Figs. 4a and 6, the calculated collapse deformation was larger than the measured value at the later stage of the process, which may be related to the increased deformation caused by the defined damage. Furthermore, the continued diffusion of water increased the degree of damage, which increased the collapse deformation at the same time. In fact, the collapse deformation in the subsequent drying stage of the field test was smaller [23], while the dry stage was based on the deformation characteristics of consolidation. Some existing studies [31] have shown that there is a critical depth for collapsibility in self-weight collapsible loess and that the collapse of loess below the critical depth significantly reduces. It can be concluded that the calculation of collapse deformation using the proposed calculation procedure overestimated the effect of water on the collapsible deformation.

In addition, it can be seen from Fig. 5c and d that the damage was relatively large, and its value lay within the range of 0.7–1.0 in the severely damaged section. According to some existing studies, the original loess undergoes collapse deformation after loading and soaking, while at the same time, the new structure regenerates [5]. When the new structure and the collapsing structure interact, the softening and hardening occur in the collapsing phenomenon, and the collapse deformation will gradually decrease. However, in simple terms, it can be assumed that the damage will inevitably cause the overestimation of the contribution of structural damage to collapsibility. Consequently, both the elastoplastic damage model and the program need to further optimize the design.

5.3 Hysteresis characteristics of the collapse deformation

Comparing Figs. 2 and 3, it can be deduced that, when the water was soaked for 16 d, it infiltrated 6 m downward, while the vertical displacement was only around 3 m. When the water was soaked for 76 d, the water infiltration was 24 m downward, while the vertical displacement was well within 14 m. Similar results were found in other calculations, which are not listed in the current paper due to limitation of space. A more detailed analysis of these calculations can be found in another study [31]. It can be seen that the generation of vertical displacement lagged behind the water infiltration and that it was not the water that infiltrated the loess and wetted it immediately. With the passage of time, the occurrence of collapse clearly exhibited its hysteresis characteristics.

Generally, the original loess has an overhead structure, which also constitutes a microstructure [12]. Both the instability and the damage of microstructure are closely related to the rigidity and stress state of the structure [24]. The water infiltration leads to gradual destruction of the microstructure. It is well known that the collapsibility of undisturbed loess is closely related to its structure, due to which the undisturbed loess has the ability to resist external loads. This ability has a positive impact on the collapse deformation. Through the CT mesoscopic scans during the water soaking process, it was found that the original structure of loess was destroyed depending on the degree of soaking [38]. In addition, during the process of loess

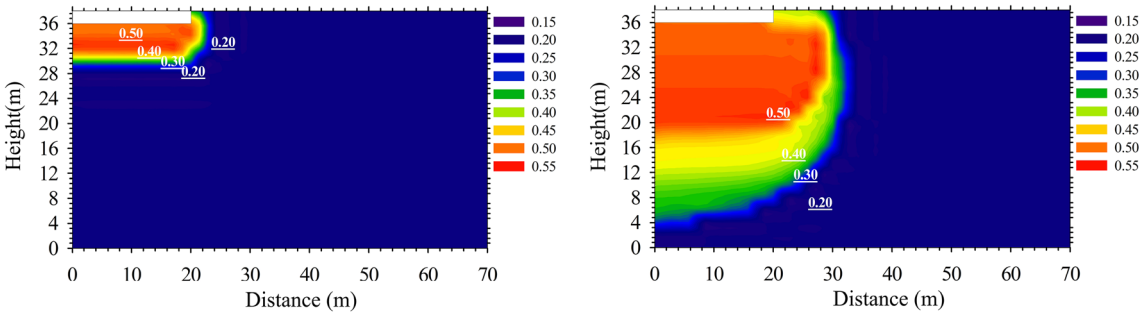

Fig. 7 Contours of moisture field in the infiltration zone when the air seepage coefficients had constant values

collapse, only when the water content reaches the critical threshold, loess collapsibility could occur [5]. It can be deduced that these factors jointly determine the hysteresis of collapsible deformation after water immersion. There are many factors affecting the hysteresis effect of collapsible deformation, and further work is required to understand this phenomenon in a better way.

5.4 Effect of unsaturated permeability/air seepage coefficients on infiltration

Unsaturated permeability and air seepage coefficients vary with the matric suction and are taken into account during the proposed design. For comparison, the air seepage coefficient was set to a constant value and did not change with the matric suction. Its value was 1.5×10^{-5} cm/s, while the step size was set to be 15 d, and the calculations were conducted 10 times. Only a few of the calculation steps are shown in Fig. 7. It can be seen that the volumetric moisture content of the infiltration zone was nearly identical to that of the infiltration zone range (as shown in Fig. 2), when water was immersed for 16 d, which indicated that the air seepage coefficient had little effect on the wetting front during the early stage of water soaking. However, when the water was immersed for 76 d, the wetting front migrated 32 m downward and 12 m to the right side (the distance from vertical line of the test pit) for constant air seepage coefficient. For unsaturated air seepage coefficient (as shown in Fig. 2) and water seepage for 76 d, the wetting front migrated 26 m downward and 12 m to the right side.

The results showed that the saturated and unsaturated air seepage coefficients had a certain influence on the calculated results for the initial wetting stage. However, this effect was not very obvious. The effect of unsaturated air seepage coefficient on the moisture transfer was mainly reflected in the middle wetting and subsequent drying stages. In the initial wetting stage, water diffused downward due to the gravity and matric suction, while the gas was discharged normally. However, when the upper loess collapsed and the pore structure was destroyed, it became difficult for the gas in pores to be discharged when it moved downward and laterally. Moreover, in the unsaturated region of the infiltration zone, with the increase in saturation and the decrease in suction, the unsaturated air seepage coefficients decrease, and the difficulty of water entering the pore increases, which makes the gas flow more difficult. This phenomenon becomes more obvious in the subsequent drying stage [9, 25].

However, when the air seepage coefficient was constant, the gas flow was no longer constrained by the factors, such as matric suction and degree of saturation, whereas the

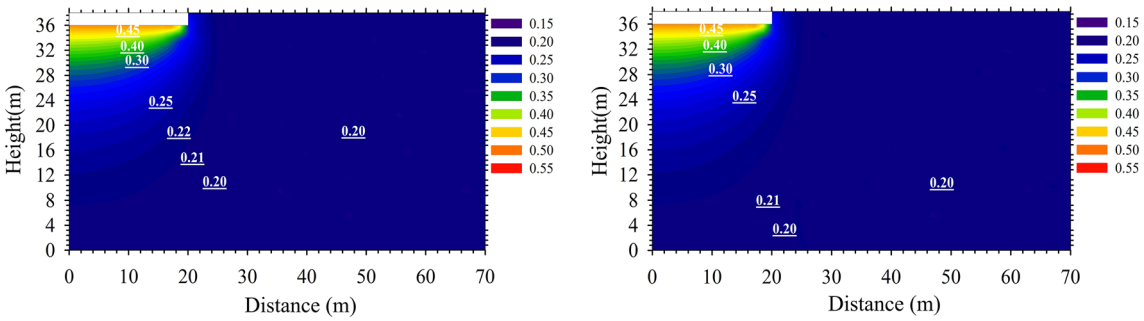

Fig. 8 Contours of moisture field when the permeability/air seepage coefficients had constant values

effect of impeding moisture migration was also not obvious [15]. Furthermore, the higher the saturation, the slower the gas flows. When the air seepage coefficient was constant, for the soil with higher degree of saturation, the gas flow rate was the same as that when the saturation was low. The gas flow sped up, while the water flow naturally accelerated. This was also the reason why the infiltration depth (shown in Fig. 7) was larger than that shown in Fig. 2b.

In the calculations, the permeability and air seepage coefficients were set to be constant, due to which both of them did not change with the variation in matric suction. The saturated permeability and air seepage coefficients had the values of 1.5×10^{-5} cm/s and 6.0×10^{-5} cm/s, respectively. The initial conditions for the model remained unchanged. Figure 8 shows the variation in volumetric water content with time for constant permeability and air seepage coefficients. When the water was immersed for 16d, it moved quickly downward, achieving the maximum depth of 28 m. The volumetric water content in the infiltration zone above the section was higher than 0.20 cm^3/cm^3, while the width of infiltration zone exceeded the test pit edge by 4 m. The infiltration zone expanded slightly when the water was immersed for 76d. It meant that the water diffusion rate was very high at the beginning of soaking, due to which it became more difficult for the moisture to diffuse in the middle and later stages of the process. The permeability coefficient was not constrained by the matric suction, and therefore, water diffused rapidly downward under the action of gravity in a short time. With the collapse deformation at the bottom of the test pit, the loess became dense and hindered further diffusion of moisture in the test pit. However, more work is needed to adequately understand this phenomenon.

6 Summary and conclusions

There are only a few studies on the multi-field coupling response of self-weight collapsible loess foundation during the wetting and drying periods. Hence, based on the BBM of unsaturated soil, an EDM of unsaturated undisturbed loess has been developed, which could respond to the damage evolution properties of undisturbed loess in the loading and collapsing process. Then, the EDM is incorporated into the unsaturated seepage consolidation coupling theory, and combining with water and air migration phenomena, an EDSCM has been established for unsaturated loess. The corresponding expressions of the new EDSCM in the plane coordinate are given in this paper. Using the Galerkin method, the key control equations have been discretized in both the space and time domains. Based on the new established EDSCM, a new finite element program termed as the ULEDSC has been compiled. The validation of the new compiled program ULEDSC has been carried out by comparing its simulated results with the monitoring data from the in situ soaking test located at Heping town, Lanzhou city, Gansu Province in China.

The numerical results show that the propagation of wetting front is identical to a pumpkin-shaped zone. It may be related to lower unsaturated permeability and the gas resistance effect. With water infiltrating slowly, the loess collapses and the vertical displacement occurs due to the self-weight of the collapsible loess and water. The vertical displacement during the subsequent drying stage is mainly caused by the consolidation settlements of the shallow soil layer below the bottom of the test pit. The occurrence of the damage is closely related to the deformation and volumetric water content, which reflects the effect of water on the structural damage. The collapsible deformation clearly exhibits hysteresis characteristics. Furthermore, only when the water content reaches the critical threshold, loess collapsibility could occur. The unsaturated air seepage coefficients had a certain influence on the calculated results for the initial wetting stage. However, this effect was not very obvious. The effect of unsaturated air seepage coefficient on the moisture transfer was mainly reflected in the middle wetting and subsequent drying stages.

The numerical results obtained from ULEDSC are in accordance with the field monitoring data, which also show the multi-field coupling response in the self-weight collapsible loess foundation during the initial wetting and subsequent drying periods. The new EDM and EDSCM could provide a scientific reference for engineering construction for collapsible loess, and the ULEDSC is a powerful tool for understanding the multi-field coupling problem of self-weight collapsible loess in Midwestern China.

Acknowledgements This work was supported by the National Natural Science Foundation of China (Grant Nos.11972374, 51509257).

References

1. Alonso EE, Gens A, Josa A (1990) A constitutive model for partially saturated soils. Géotechnique 40(3):405–430
2. Chang CS, Duncan JM (1983) Consolidation analysis for partly saturated clay by using an elastic-plastic effective stress-stating model. Int J Numer Anal Meth Geomech 17(7):39–55
3. Chen ZH (1993) Consolidation theory of unsaturated soil based on the theory of mixture(II). Appl Math Mech (Engl Edit) 14(8):137–150
4. Chen ZH (1999) Deformation, strength, yield and moisture change of a remolded unsaturated loess. Chin J Geotech Eng 21(1):82–90
5. Chen ZH, Xu ZH, Liu ZD (1986) Some problems of collapsed loess (in Chinese). Chinese Journal of Civil Engineering 19(3):62–69
6. Chen ZH, Huang H, Lu ZH (2001) Nonlinear and elasto–plasticity consolidation models of unsaturated soil and applications. Appl Math Mech (Engl Edit) 22(1):105–117

7. Costa LM, Pontes IDS, Guimarães LJN, Ferreira SRM (2008) Numerical modelling of hydro–mechanical behaviour of collapsible soils. Int J Numer Methods Biomed Eng 24(12):1839–1852
8. Desai CS, Toth J (1996) Disturbed state constitutive modeling based on stress–strain and nondestructive behavior. Int J Solids Struct 33(11):619–1650
9. Dixon RM, Linden DR (1972) Soil air pressure and water infiltration under border irrigation1. Soil Sci Soc Am J 36(6):948–953
10. Fang XW, Chen ZH, Shen CN, Sun SG (2004) A study on effect of shear on soil–water characteristic curve. Rock Soil Mech 25(9):1451–1454
11. Gao GR (1981) Classification of microstructures of loess in china and their collapsibility. Sci China Math 24(7):962–974
12. Gao G (1988) Formation and development of the structure of collapsing loess in China. Eng Geol 25(2–4):235–245
13. Gvirtzman H, Shalev E, Dahan O, Hatzor YH (2008) Large-scale infiltration experiments into unsaturated stratified loess sediments: monitoring and modeling. J Hydrol 349(1–2):214–229
14. Habibagahi G, Mokhberi M (1998) A hyperbolic model for volume change behavior of collapsible soils. Can Geotech J 35(2):264–272
15. Hachum AY, Alfaro JF, Willardson LS (1976) Water movement in soil from trickle source. J Irrig Drain Div 102(2):179–192
16. Haeri SM (2016) Hydro-mechanical behavior of collapsible soils in unsaturated soil mechanics context. Jpn Geotech Soc Spec Publ 2(1):25–40
17. Huang XF, Li J, Cui H, Li JG (2010) Distribution characteristics of earth pressure for unsaturated intact loess. Chin J Geotech Eng 32(4):500–506
18. Jiang MJ, Li T, Hu HJ, Thornton C (2014) DEM analyses of one-dimensional compression and collapse behaviour of unsaturated structural loess. Comput Geotech 60(1):47–60
19. Li XK, Zienkiewicz OC (1992) Multiphase flow in deforming porous media and finite element solutions. Comput Struct 45(2):211–227
20. Liu MD, Carter JP (2002) A structured Cam Clay model. Can Geotech J 39(6):1313–1332
21. Liu E, Yu HS, Deng G, He S (2014) Numerical analysis of seepage-deformation in unsaturated soils. Acta Geotech 9(6):1045–1058
22. Lu ZH, Chen ZH, Fang XW, Guo JF, Zhou HQ (2006) Structural damage model of unsaturated expansive soil and its application in multi-field couple analysis on expansive soil slope. Appl Math Mech (Engl Edit) 27(7):891–900
23. Ma Y, Wang JD, Peng SJ (2013) Immersion tests on characteristics of deformation of self-weight collapsible loess under overburden pressure. Chin J Geotech Eng 36(3):537–546
24. Miao T, Liu Z, Niu Y (2002) Unified catastrophic model for collapsible loess. J Eng Mech 128(5):595–598
25. Moon S, Nam K, Kim JY, Hwan SK, Chung M (2008) Effectiveness of compacted soil liner as a gas barrier layer in the landfill final cover system. Waste Manag 28(10):1909–1914
26. Rotisciani GM, Sciarra G, Casini F, Desideri A (2015) Hydro–mechanical response of collapsible soils under different infiltration events. Int J Numer Anal Meth Geomech 39(11):1212–1234
27. Suebsuk J, Horpibulsuk S, Liu MD (2010) Modified structured Cam Clay: a generalized critical state model for destructured, naturally structured and artificially structured clays. Comput Geotech 37(7):956–968
28. Van Genuchten MTh (1980) A closed-form equation for predicting the hydraulic conductivity of unsaturated soils. Soil Sci Soc Am J 44(5):892–898
29. Wang ZG, Kang GJ, Ma CW, Miao T (1994) A study on the generating mechanism of vertical joints in loess. Sci China Chem 37(2):250–256
30. Wu XP, Wang LM, Fang JH, Xu AH, Zhou YL, Zhao YH (2018) Seepage characteristics and their relationship with self-weight collapse of intact loess ground. Chin J Geotech Eng 40(6):1002–1009
31. Yao ZH (2012) Water–air migration, mechanical characteristics and foundation collapse deformation of self–weight collapse loess with heavy section (in Chinese). Ph.D. dissertation. Logistic Engineering University
32. Yao YP, Zhou AN (2013) Non-isothermal unified hardening model: A thermo-elasto-plastic model for clays. Geotechnique 63(15):1328–1345
33. Yao YP, Sun DA, Matsuoka H (2008) A unified constitutive model for both clay and sand with hardening parameter independent on stress path. Comput Geotech 35(2):210–222
34. Yao YP, Hou W, Zhou AN (2009) UH model: three-dimensional unified hardening model for overconsolidated clays. Geotechnique 59(5):451–469
35. Yao ZH, Huang XF, Chen ZH, Zhang JH (2012) Comprehensive soaking tests on self-weight collapse loess with heavy section in Lanzhou region. Chin J Geotech Eng 34(1):65–74
36. Yao ZH, Chen ZH, Huang XF, Zhang SJ, Yang XH (2012) Hydraulic conductivity of unsaturated undisturbed and remolded Q_3 loess. Chin J Geotech Eng 34(6):1020–1027
37. Yao ZH, Chen ZH, Huang XF, Qin XH, Zhang JH (2012) Experimental research on gas permeability of unsaturated Q_3 loess. Chin J Rock Mech Eng 31(6):1264–1273
38. Zhu YQ (2008) Constitutive model of undisturbed collapsible loess based on meso-structure change. Ph.D. dissertation: Logistic Engineering University
39. Zhu EY, Yao YP (2015) Structured UH model for clays. Transp Geotech 3:68–79